Signal Compensation and Compressed Sensing for Magnetization-Prepared MR Angiography

Tolga Çukur*, *Member, IEEE,* Michael Lustig, *Member, IEEE,* Emine U. Saritas, *Member, IEEE,* and Dwight G. Nishimura, *Member, IEEE*

***Abstract*—Magnetization-prepared acquisitions offer a trade-off between image contrast and scan efficiency for magnetic resonance imaging. Because the prepared signals gradually decay, the contrast can be improved by frequently repeating the preparation, which in turn significantly increases the scan time. A common solution is to perform the data collection progressing from low- to high-spatial-frequency samples following each preparation. Unfortunately, this leads to loss of spatial resolution, and thereby image blurring. In this work, a new technique is proposed that first corrects the signal decay in high-frequency data to mitigate the resolution loss and improve the image contrast without reducing the scan efficiency. The proposed technique then employs a sparsity-based nonlinear reconstruction to further improve the image quality. In addition to reducing the amplified high-frequency noise, this reconstruction extrapolates missing k-space samples in the case of undersampled compressed-sensing acquisitions. The technique is successfully demonstrated for non-contrast-enhanced flow-independent angiography of the lower extremities, an application that substantially benefits from both the signal compensation and the nonlinear reconstruction.**

***Index Terms*—Angiography, compensation, compressed sensing, magnetization preparation, MRI, signal decay.**

I. Introduction

GRADIENT-echo (GRE) sequences provide significantly faster acquisitions compared with spin-echo sequences [1], and have found wide use in numerous magnetic resonance imaging (MRI) applications such as three-dimensional (3D) imaging [2], coronary imaging [3], [4], angiography [5], functional MRI [6], and hyperpolarized imaging [7], [8]. However, because data are acquired while the magnetization is in a dynamic equilibrium known as steady state, GRE demonstrates different signal characteristics than spin-echo sequences. Furthermore, the direct application of conventional contrast-generation methods (e.g., inversion recovery, T_2-preparation) would substantially prolong the repetition times (TR) of GRE sequences, taking away their speed advantage.

This work was supported in part by the National Institutes of Health under Grant R01-HL39297 and Grant R01-HL075803, and in part by GE Healthcare. *Asterisk indicates the corresponding author.*

*T. Çukur is with the Helen Wills Neuroscience Institute, University of California, Berkeley, CA 94720 (e-mail: cukur@berkeley.edu). M. Lustig is with the Department of Electrical Engineering and Computer Sciences, University of California, Berkeley, CA 94720. E. U. Saritas is with the Department of Bioengineering, University of California, Berkeley, CA 94720. D. G. Nishimura is with the Department of Electrical Engineering, Stanford University, Stanford, CA 94305.

To maintain both the desired contrast and the acquisition speed, the signals generated by magnetization-preparation modules are usually captured with GRE host sequences [9], [10]. Unfortunately, the initial contrast is progressively replaced by the lower steady-state contrast in such transient acquisitions. Therefore, after a single preparation, only a limited amount of k-space data can be collected with the desired contrast.

Magnetization-prepared sequences often employ two complementary strategies to address this issue. First, segmented k-space acquisitions can be performed, where the preparation is repeated multiple times for complete coverage and each segment is followed by a magnetization-recovery period. Increasing the number of segments enhances the image contrast, but degrades the scan efficiency due to the preparation overhead. Although prolonged scan times can be avoided with the help of acceleration techniques such as parallel imaging [11], [12], large undersampling factors are necessary. This can result in reduced SNR, as well as residual undersampling artifacts.

Second, the captured signal for each shot can be enhanced with centric phase-encode ordering, since the energy in MR images is mostly concentrated at low spatial frequencies [13]–[15]. However, the transient signal decay acts as a low-pass filter on the data, reducing the image resolution [13], [16]. Although variable-flip-angle schemes can improve the signal homogeneity across k-space [8], [17], this is often achieved at the expense of decreased signal and contrast levels.

In this work, we propose a simple postprocessing technique in conjunction with centric k-space acquisitions to enhance magnetization-prepared sequences. The technique compensates the k-space data for the signal decay experienced by the tissue of interest (i.e., the data are high-pass filtered to enhance the intensity of high-spatial-frequency samples). This compensation prevents image blurring in centric acquisitions without reducing the signal levels, thereby improving the spatial resolution. Furthermore, assuming the background tissues have lower spatial-frequency content than the tissue of interest (e.g., muscle vs. blood vessels), the desired tissue signal will be increased while the background level remains relatively constant. As a result, the image contrast will be enhanced without the need for prolonged scan times (i.e., increased number of segments) or large undersampling factors. Finally, the technique incorporates sparsity-enforcing reconstructions [18]–[20] to suppress the amplified noise due to higher weighting of peripheral k-space data.

The proposed technique offers significant performance im-

provements for flow-independent steady-state free precession (SSFP) angiography [21], [22], a magnetization-prepared sequence that can produce vessel images without the need for contrast agents [23]. These angiograms can suffer from image blurring due to the signal decay during centric acquisitions, and a large number of segments are required for effective capturing of the transient contrast. Correcting for the blood-signal decay addresses both problems without extending scan times. Furthermore, because angiographic datasets are inherently sparse in the spatial-finite-differences domain, sparsity-based nonlinear reconstructions can reduce the resulting noise and depict the blood vessels reliably [24].

II. Methods

Although many applications can benefit from the technique presented in this work, we specifically demonstrate the results on magnetization-prepared SSFP angiography. These SSFP sequences can produce flow-independent angiograms without contrast agents through segmented and centric k-space acquisitions [22], [25], [26]. However, because the prepared contrast gradually decays to the lower SSFP contrast, tissue signals vary across k-space [24]. More frequent preparation can improve the captured contrast by shortening the readout clusters, but it also prolongs the total scan time. Instead, we propose to enhance the image contrast and resolution without any scan-time penalties, by simply compensating for the signal decay in transient acquisitions. A sparsity-based nonlinear reconstruction is then employed to recover the blood vessels from fully-sampled and undersampled datasets [20]. While this nonlinear technique performs image denoising in the former case, it is used to simultaneously reduce noise and aliasing artifacts in the latter. Because the reconstructions in both cases are identically formulated, we will simply refer to them as compressed sensing (CS) for the sake of brevity and coherence.

The following sections provide a brief overview of the magnetization-prepared pulse sequence, and describe the signal-compensation scheme along with the sparsity-enforcing CS reconstructions. Afterward, the simulations and in vivo experiments performed to demonstrate the technique are outlined.

A. Pulse Sequence

In lower-extremity MR angiograms, fat and muscle tissues are the two major constituents of the background signal. The fat signal can be effectively suppressed with an alternating repetition time (ATR) SSFP host sequence [26], [27]. Meanwhile, T_2-preparation with an adiabatic BIR-4 pulse is employed to reduce the muscle signal [28]. However, because the generated contrast is transient, the capturing efficiency is enhanced by performing centric phase-encode ordering on a square-spiral trajectory [29]. The diagram of the magnetization-prepared sequence is shown in Fig. 1. Immediately following T_2-preparation, a ramped series of RF excitations dampens the transient signal oscillations [30], [31]. All data samples within a given segment are then acquired with the host sequence. Finally, the magnetization is allowed to relax during a recovery period. This entire module is repeated to collect each k-space segment.

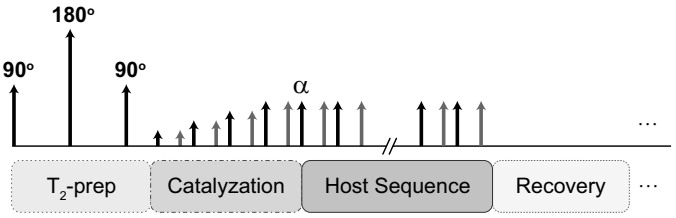

Fig. 1. Pulse sequence diagram of the magnetization-prepared SSFP sequence. A T_2-preparation is performed at the beginning of each k-space segment, followed by a ramped series of RF excitations to dampen the transient signal oscillations. Afterward, data are acquired with an ATR SSFP host sequence. Because the prepared contrast gradually decays to the steady-state contrast, only a limited number of samples are collected after a single preparation. The magnetization is then allowed to recover during a certain time period. This procedure is repeated until all segments are acquired.

B. Signal Compensation

The proposed technique can improve contrast if the tissue of interest has higher spatial-frequency content than the background. This condition is effectively satisfied for lower-extremity angiograms, where relatively thin blood vessels are paired with large blocks of skeletal muscle tissue. The axial cross-section of a simple numerical lower-leg phantom is shown in Fig. 2a. The individual spatial-frequency contents (i.e., spectral widths) can be computed by first separating the phantom into its blood and muscle components (Fig. 2b). The corresponding k-space representations (i.e., Fourier transforms) clearly demonstrate that vessels contribute more heavily to high-spatial-frequency data (e.g., $k_{rad} > 0.2$, where k_{rad} is the k-space radius) than muscle, due to their finer structures.

To illustrate the effects of compensation on the image quality, we can closely analyze the acquired MR signal:

$$Y(k) = \int_{Volume} m_{\perp}(r,t)\, e^{-j2\pi k \cdot r}\, dV \; + \; N(k), \quad (1)$$

where $k = K_s(t)$ denotes the k-space location vector as a function of time, r is the spatial coordinate vector, and $N(k)$ is a bivariate white Gaussian noise term. $m_{\perp}(r,t)$, the spatio-temporal distribution of the transverse magnetization, can be written as the summation of the individual tissues' contributions:

$$m_{\perp}(r,t) = \sum_{tissues} \big\{ M_{tran}(t) \cdot i(r) \big\}. \quad (2)$$

Here, $M_{tran}(t)$ represents the transient magnetization level, which depends on the $T_{1,2}$ of each tissue as well as the sequence parameters. Meanwhile, $i(r)$ is the image mask that describes the spatial distribution of each tissue (e.g., the component masks in Fig. 2b). This decomposition allows us to separately analyze the spatial and temporal variations of the transverse magnetization.

To express the acquired signal in k-space, the variation of blood and muscle magnetization levels was derived as a function of k. First, the transient magnetization, $M_{tran}(t)$,

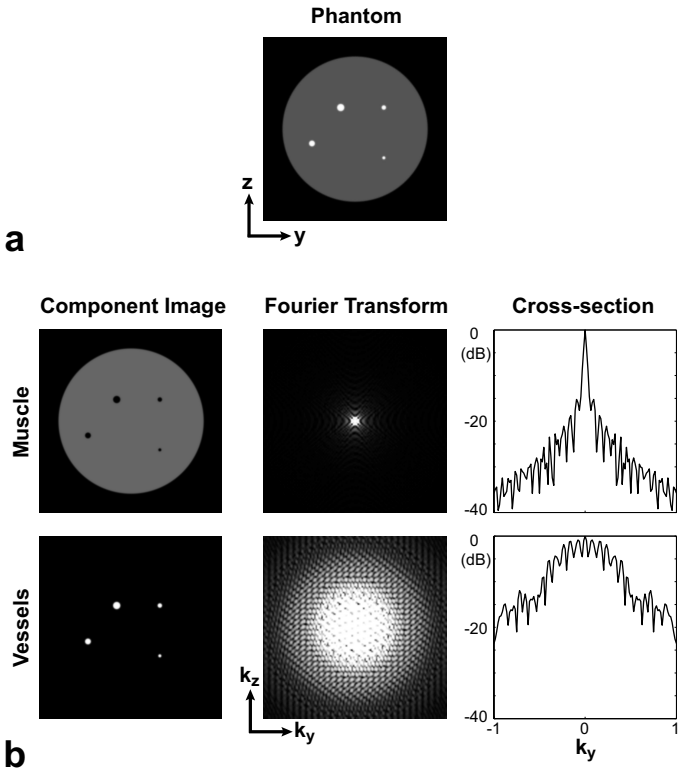

Fig. 2. **(a)** A numerical phantom simulating a simple cross-sectional model of the lower leg in the axial plane. The muscle signal is depicted with gray color, whereas the four blood vessels of varying diameters are shown as white. **(b)** The phantom was deconstructed into its two tissue components (left column), namely muscle and blood vessels in the upper and lower rows respectively. The spectral-domain (i.e., k-space) representation of each component image was computed separately with a two-dimensional Fourier transform (center column). The central cross-sections of the Fourier transforms are also visualized (right column). All spectra in **b** are normalized to yield a maximum amplitude of unity, and shown in logarithmic scale with identical display windowing. As clearly observed, the spectrum for the blood-vessel image is much broader than that for the muscle image. Because the vessels have smaller structures, they have significantly increased high-frequency content compared to the large muscle tissue.

following catalyzation was computed with Bloch simulations. Assuming the magnetization vector has been aligned with its steady-state direction after catalyzation, the decay of the transient magnetization can be stated as [30], [32]:

$$M_{tran}(t) = (M_{prep} - M_{ss}) \cdot \tau^{t/TR} + M_{ss}, \qquad (3)$$

where M_{prep} and M_{ss} denote the initially prepared and steady-state magnetizations, and $t = n \cdot TR$ for $n \in \mathbb{N}$. The exact mathematical expression of the decay rate, τ, is fairly complicated for ATR SSFP. Nonetheless, the empirical decay characteristics of ATR are reasonably similar to that of regular SSFP, which is a weighted average between pure T_1 and T_2 decays for on-resonant spins [32]. The k-space trajectory is also as a function of time, $K_s(t)$, given the sampling pattern and the number of k-space segments. Finally, we can compute $M(k)$, the tissue magnetization during the acquisition of a corresponding k-space sample:

$$M(k) = M_{tran}({K_s}^{-1}(k)), \qquad (4)$$

where ${K_s}^{-1}$ represents the inverse mapping $t = {K_s}^{-1}(k)$.

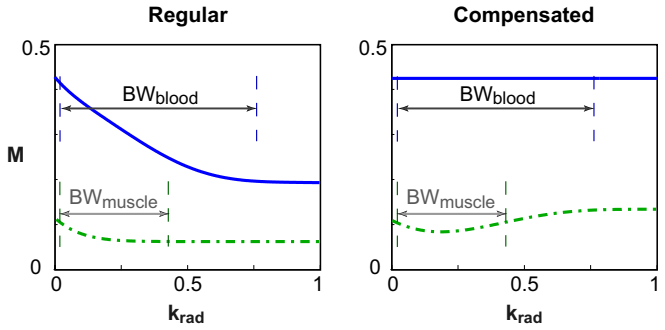

Fig. 3. Blood (T_1/T_2 = 1200/250 ms) and muscle (870/50 ms) magnetizations following T_2-preparation as a function of k-space radius (k_{rad}). The initial blood/muscle contrast of ~ 5, decays to ~ 3 in steady-state. The illustrative spatial-frequency extents (BW) of these two tissues are also shown. Due to the fine structure of vessels in the extremities, the blood signal has higher spatial-frequency content compared to that of muscle. Hence, the blood signal can be increased by compensating for its decay, while the muscle signal remains roughly the same. This enhances the blood/muscle contrast and prevents the blurring of vessel images.

Approximate T_1 and T_2 values from literature [33], [34] were selected to simulate the blood magnetization across k-space. Although $T_{1,2}$ measurement routines can be incorporated for improved performance, the final results were not considerably affected by small variations in parameter values according to our observations. Furthermore, accurate estimation of these parameters often requires substantial scan times. The following relaxation parameters were used in the simulations: T_1/T_2 = 1200/250 ms for blood [33], [34], and T_1/T_2 = 870/50 ms for muscle [35] at 1.5 T. Meanwhile, the corresponding sequence parameters were $\alpha = 60^o$, $TR_1/TR_2/TE$ = 3.45/1.15/1.725 ms, 80-ms T_2-preparation time, 8 k-space segments, and a 10-excitation catalyzation sequence. The tissue contrast at the start of the acquisition is a complicated function of the T_2-preparation time, the catalyzation sequence, and the tip angle of the host sequence. These parameters were chosen to maximize the initial blood/muscle contrast in the lower extremities at 1.5 T, without exceeding specific absorption rate limits.

The T_2-preparation generates higher levels of magnetization and improved T_2-contrast compared to regular SSFP, as displayed in Fig. 3. Whereas the blood/muscle contrast reaches as high as $\sim$5 initially, the host sequence drives the magnetization levels to a steady-state where the contrast decays to $\sim$3. In the absence of compensation, this reduces the captured contrast particularly at high spatial frequencies. On the other hand, the morphological differences between vessels and muscle are especially pronounced in the axial cross-section of the lower leg, which coincides with the two phase-encoding directions (left/right and anterior/posterior) in our 3D acquisitions. Therefore, the blood signal can be effectively increased by compensating for its decay over the phase-encoding k-space dimensions, while the muscle signal remains relatively unaltered due to its lower spatial-frequency content.

To better understand the effects of compensation, we can examine the k-space variation of the acquired signal by com-

bining (1), (2), and (4). Assuming blood and muscle tissues are the only constituents for simplicity:

$$Y(k) = \int \left[M_b(k) \cdot i_b(r) + M_m(k) \cdot i_m(r)\right] e^{-j2\pi k \cdot r}\, dV + N(k), \tag{5}$$

where $M_{b,m}(k)$ are the magnetizations and $i_{b,m}(r)$ are the spatial distributions of the blood and muscle tissues. Because $M_{b,m}(k)$ do not depend on r, the integrals with complex-exponential kernels are equivalent to evaluating the Fourier transforms of $i_{b,m}(r)$ at a given k-space location, i.e., $I_{b,m}(k)$,

$$Y(k) = M_b(k) \cdot I_b(k) + M_m(k) \cdot I_m(k) + N(k). \tag{6}$$

The k-space compensation filter is computed for a desired tissue of interest, which is arterial blood in angiographic datasets. The filter weights, $H(k)$, are inversely proportional to the level of blood magnetization, $|M_b(k)|$, at each k-space location:

$$H(k) = \left|\frac{M_b(0)}{M_b(k)}\right|, \tag{7}$$

where the scaling factor, $|M_b(0)|$, normalizes the filter amplitude to 1 at the center of k-space. The compensation is achieved by multiplying the k-space data, $Y(k)$, with this filter,

$$Y_{comp}(k) = M_b(0)\cdot I_b(k) + H(k)\cdot M_m(k)\cdot I_m(k) + H(k)\cdot N(k). \tag{8}$$

As expected, the filter effectively compensates for the blood-signal decay. Because muscle tissue has low spatial-frequency content (i.e., $I_m(k) \ll I_m(0)$ for $\mathrm{k_{rad}} > \mathrm{k_{ro}}$, where $\mathrm{k_{ro}}$ is considerably small) and the filter can be crudely approximated as $H(k) \approx 1$ for $\mathrm{k_{rad}} < \mathrm{k_{ro}}$, the compensation does not affect the muscle signal significantly:

$$Y_{comp}(k) \approx M_b(0)\cdot I_b(k) + M_m(k)\cdot I_m(k) + H(k)\cdot N(k). \tag{9}$$

Meanwhile, $H(k)$, a monotonically increasing function, amplifies the noise at high spatial frequencies as a side effect.

The signal compensation enhances the quality of the angiograms in two major aspects. First of all, because the blood signal is increased relative to the muscle signal, the overall blood/background contrast is improved. Furthermore, correcting for the blood-signal decay prevents potential loss of spatial resolution in transient acquisitions.

C. Compressed Sensing

Following the compensation, the high-spatial-frequency data are weighted more heavily, which causes regular Fourier reconstructions to suffer from increased image noise. This will not pose a problem when the precompensation SNR levels are relatively high (e.g., SNR $\gtrsim$ 40), as decent image quality can still be maintained. Nonetheless, the reconstructions can benefit from complementary noise-reduction schemes in other cases. While numerous effective denoising techniques have been proposed [36], compressed sensing is a particularly attractive candidate for MR angiograms. First, many denoising algorithms rely heavily on redundancies in the data, and CS can readily exploit the high degree of sparsity in angiograms. In addition, undersampling allows the quality of the angiograms to be significantly enhanced without increasing sensitivity to patient motion, improving their clinical utility. Therefore, flow-independent angiography can further benefit from the ability of CS to reconstruct undersampled acquisitions.

The theory of CS states that a nonlinear reconstruction can recover a signal of size L from only η of its samples (where $\eta \ll L$) if several conditions are met. First of all, the signal should be compressible. A signal of size L is denoted as compressible if it can be accurately represented by $\eta \ll L$ coefficients of a linear transform (e.g., spatial finite differences, Fourier transform, wavelet transform). An angiographic dataset is highly compressible in the image domain, and its total variation (i.e., sum of spatial finite differences) has an even sparser representation [20], [24].

In addition, the aliasing artifacts due to the missing samples should be incoherent in the transform domain. When undersampled acquisitions were performed in this work, this condition was satisfied by employing variable-density random undersampling in the phase-encode plane [20], [24]. First, a probability density function was constructed with a gradually diminishing density towards the edge of k-space. This function was then used to generate a random sampling pattern through a Monte Carlo procedure. It is important to note that random undersampling can cause variations in the blood-magnetization level among separate k-space segments, which are more pronounced at higher undersampling factors (R) and in the periphery of k-space. We calculated the percentage difference between the highest and lowest magnetizations at each $\mathrm{k_{rad}}$ for the trajectories employed in this work. Even with R = 4, the maximum and mean differences across k-space were limited to 11.7% and 6.7% respectively, and the differences in central k-space were negligible. Nevertheless, to prevent potential image artifacts due to abrupt variations in the filter values, a smooth filter was designed based on the minimum level of blood magnetization at a given $\mathrm{k_{rad}}$ among all segments.

Finally, the reconstruction must simultaneously enforce the compressibility of the image and its consistency with the acquired data. This can be achieved through solving the following unconstrained nonlinear optimization,

$$minimize \quad ||W \cdot (F_u m - H \cdot Y)||_2 + \lambda_1 ||m||_1 + \lambda_2 TV(m)$$

The first term is the weighted ℓ^2-norm difference between the reconstructed data and the compensated k-space acquisitions, $F_u m$ and $H \cdot Y$ respectively. This data-consistency term is accompanied by two regularization terms in the objective, the ℓ^1-norm of the image, m, and its total variation, $TV(m)$. Because the reconstructions are performed only on the phase-encoding dimensions in this work, F_u denotes a partial Fourier operator. The outlined optimization produces the most likely coefficient estimates in the transform domain subject to the data-consistency constraint. When the aforementioned conditions are satisfied, CS denoises the images while preserving the edges, thereby improving the apparent SNR.

The compensation filter, $H(k)$ (described in (7)), leads to colored noise in the data. A weighting factor of $W(k) = \{H(k)\}^{-1}$ would then result in uniform weighting of the

noise-related ℓ^2-norm error contributions across k-space. However, this also places a higher emphasis on enforcing data consistency at lower spatial frequencies, counteracting the effects of signal compensation. Instead, $W(k) = 1$ was employed for the reconstructions in this work, yielding 4-7% improvement in blood/muscle contrast for in vivo angiograms, with no notable differences in the noise/artifact levels.

The implementation details of the algorithm are described in Ref. [24]. The objective was minimized using a nonlinear conjugate-gradient technique [20]. ℓ^1-norm reconstructions can shrink (i.e., underestimate) the coefficients pertaining to low-contrast image features, further reducing their contrast. A sufficiently small λ_1 was chosen to minimize the shrinkage effects while still enforcing sparsity. In addition, excessive TV regularization can lead to image flattening (i.e., block artifacts) and loss of small-sized image features. Therefore, a relatively small λ_2 was used to mitigate such artifacts while effectively denoising the images. λ_1 = 0.05 and λ_2 = 0.025 were observed to yield good-quality reconstructions.

D. Simulations

The levels of improvement in image contrast and spatial resolution depend on several sequence and tissue parameters. First, the number of k-space segments (N) or the undersampling factor (R) can change the signal variation with k_{rad}, even if the remaining parameters are kept constant. For smaller N and R, the initial portion of the magnetization-decay curve is steeper as shown in Fig. 4. This leads to greater resolution and contrast reduction in the original acquisitions. The compensation filter then weights a greater portion of higher-spatial-frequency data more heavily. Therefore, highest levels of improvement are achieved for smaller number of segments and acceleration factors, i.e., longer readout clusters. The contrast is also affected by the relative spatial-frequency contents of the two tissues. Because high frequencies are weighted more heavily compared to the center of k-space, the enhancement will be higher when the filter minimally alters the muscle signal (i.e., larger and more homogeneous blocks of muscle tissue). On the other hand, the blood signal benefits increasingly from the high-frequency amplification as the vessel sizes get smaller. Finally, because the compensation filter is designed using *a priori* estimates of relaxation parameters, any variations in $T_{1,2}$ (e.g., spatial or inter-subject) can change the actual contrast levels.

Another factor that impacts the image quality is the sparsity-based nonlinear reconstruction. By nature, CS will demonstrate enhanced performance on more compressible datasets. Whereas the compensation produces sparser images by reducing the background signal, the amplification of high-frequency noise increases the background variation. As a result, the reliability of noise/artifact removal inherently depends on the relative balance between these two counteracting components.

Several simulations were performed to assess the aforementioned relationships regarding contrast, resolution, and reconstruction performance as described in the following subsections.

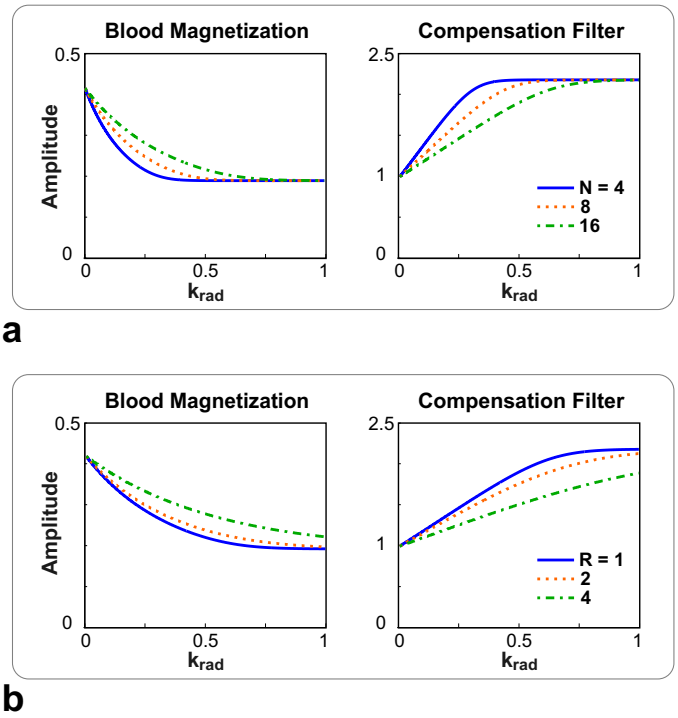

Fig. 4. Transverse blood magnetization (T_1/T_2 = 1200/250 ms) and the corresponding compensation filter as a function of k-space radius (k_{rad}), simulated for varying number of k-space segments (N) and undersampling factors (R). **(a)** N = (4,8,16) for a fixed R = 1, **(b)** R = (1,2,4) for a fixed N = 16. Because the readout clusters are lengthened for smaller N and R, the decay of the blood magnetization is steeper. In order to compensate for this decay, the filters weight a greater portion of higher-spatial-frequency data more heavily.

1) Contrast: To demonstrate the effects of the number of segments and the vessel diameter, contrast measurements were performed on the numerical lower-leg phantom (Fig. 2a). This phantom was constructed by modeling muscle tissue and blood vessels with circular cross-sections in the axial plane for simplicity. The average luminal diameters of the major deep vessels in the lower leg range approximately from 2 to 4 mm [37], [38], while small vessel branches could be narrower. Therefore, the phantom included four vessels with diameters of 1, 2, 3, and 4 mm respectively, and the diameter of the muscle tissue was 100 mm. The axial phantom images covered a 128×128-mm^2 field-of-view sampled with a 1024×1024 matrix. Two image masks, $i_{b,m}(r)$ (r denoting the spatial coordinate), were formed to separate the blood and muscle components, respectively. To avoid abrupt signal transitions, a Fermi window was used to provide a 4-pixel-wide transition on the periphery of each circular structure.

Magnetization-prepared phantom images were produced by first simulating the blood and muscle magnetizations, $M_{b,m}(k)$, with respect to k-space location (k_y-k_z) as described in the Methods section (Fig. 3). These magnetizations were sampled on a 128×128 grid to yield a nominal isotropic resolution of 1 mm:

$$\widehat{M}_{b,m}(k) = M_{b,m}(k) \cdot \sum_i \delta(k - k_i), \qquad (10)$$

where k_i denote the discrete sampling locations in the phase-encode plane. Afterward, the Fourier transforms of the image masks, $I_{b,m}(k)$, were sampled on the same grid. To compute the contribution from each component, the Fourier transform of its mask was multiplied with the corresponding magnetization. These contributions were then summed to simulate the acquired k-space data:

$$\widehat{Y}(k) = \widehat{M}_b(k) \cdot \widehat{I}_b(k) + \widehat{M}_m(k) \cdot \widehat{I}_m(k). \qquad (11)$$

The data, $\widehat{Y}(k)$, were reconstructed without and with compensation for the blood-signal decay. The blood/muscle contrast, i.e., the ratio of the mean blood signal to the mean muscle signal, was then quantified on regular and compensated images. Mean blood signals were measured on each vessel separately, and the entire muscle tissue was selected to calculate the mean background level.

The robustness of the compensation filter was evaluated against variations in relaxation parameters with a separate series of simulations. First, the four parameters of the numerical phantom (i.e., $T_{1,2}$ of blood and muscle tissues) were individually perturbed within the $\pm$20% range in 9 linear steps, while the rest of the parameters were kept at their nominal values. In addition, spatial variations were simulated by modeling the large block of muscle tissue as 9 concentric annuli, which were assigned different T_1 or T_2 values varying linearly in the $\pm$20% range. Blood/muscle contrast measurements were performed on regular and compensated images following the aforementioned procedure. Means and standard deviations of these measurements were computed across the axes of perturbation.

2) Resolution: Whereas the previous simulations demonstrated contrast variations, the level of resolution improvement was quantified using a measure of relative resolution based on the point spread function (PSF, i.e., the reconstructed image for an impulse object), as described in Ref. [39]. The relative resolution was assumed to be the radius of a cylinder with a height equal to the peak amplitude of the PSF, and a volume equal to the integral of the PSF. A 128×128 sampling grid was again formed in the phase-encode plane (k_y-k_z), yielding a nominal isotropic resolution of 1 mm. For various numbers of k-space segments, the variation of the blood-magnetization level was simulated as a function of k-space radius for both the regular and compensated cases as shown in Fig. 3. These magnetizations, $\{M_b(k)\}_{reg,comp}$, were separately sampled on the k-space grid, and their inverse Fourier transforms yielded the corresponding PSFs, $s(r)$. Finally, the ratio of the volume under the PSF to the peak amplitude of the PSF was computed, and the nominal resolution was quantified by the square root of this ratio,

$$\Delta r_o \propto \sqrt{\frac{\iint s(r)\, dA}{s(r=0)}}. \qquad (12)$$

3) Reconstruction Performance: To analyze the effect of compensation on the CS reconstruction, Monte Carlo simulations were performed using the numerical lower-leg phantom. Image SNR levels varying from 5 to 60 (measured on muscle tissue) were maintained by adding bivariate white Gaussian noise to magnetization-prepared data. Regular and compensated phantom images were then reconstructed. Afterward, the spatial-finite-differences transforms of both images were computed across a horizontal cross-section with two separate vessels.

An improvement in sparsity is indicated by increased peak levels of finite-differences (FD) coefficients relative to the background variation. Therefore, the FD-domain SNR (SNR_{FD}) was utilized as a performance measure for the sparsity-enforcing reconstructions. The maximum FD coefficient was normalized by the standard deviation of the background to quantify SNR_{FD}. The standard deviation was estimated as $\sigma = 0.7413 \cdot$ IQR, where IQR denotes the interquartile range of the background coefficients [40]. IQR, robust against outliers, was chosen as a more reliable dispersion metric for sparse signals than a direct measurement of σ. Sample noise generation and the following procedure were repeated 1000 times, and the results were averaged. Paired Student's t-tests were performed between the sample SNR levels of the regular and compensated cases.

E. Experiments

In vivo non-contrast-enhanced flow-independent angiograms of the lower leg were produced on a 1.5 T GE Signa EX scanner with CV/i gradients (maximum strength of 40 mT/m and slew rate of 150 T/m/s) using a quadrature transmit/receive extremity coil. The magnetization-prepared acquisitions employed a 3D Cartesian ATR SSFP host sequence. The following set of common scan parameters were prescribed: 192×128×128-mm^3 field-of-view, 1×1×1-mm^3 spatial resolution, $\alpha = 60^o$, 4.6-ms total TR (TR_1/TR_2 = 3.45/1.15 ms), 1.725-ms TE, 125-kHz readout bandwidth, 80-ms T_2-preparation, 10-tip linear ramp catalyzation, and a 4-s recovery time between consecutive segments. Meanwhile, the number of k-space segments (N), the undersampling factors (R), and the total scan times T_{scan} were varied.

Both fully-sampled and undersampled acquisitions were performed to demonstrate the proposed technique. For the fully-sampled case, 3 datasets were collected with N = (4,8,16) and corresponding T_{scan} = (88,104,137) sec, while the number of phase encodes per k-space segment were (4096,2048,1024), respectively. Although the time spent for magnetization preparation was proportional to N, the total number of phase encodes remained constant. Hence, the increase in T_{scan} was less than linear with N. As an alternative, 3 undersampled datasets were acquired with R = (1,2,4), N = (4,16,22), (4096,512,186) phase encodes per segment, and T_{scan} = 88 sec each. While the scan times were kept constant, higher undersampling factors were required to enable more frequent preparation. Four sets of images were produced from fully-sampled datasets using Fourier and CS reconstructions both without and with signal compensation. Meanwhile, undersampled data were reconstructed using CS without and with signal compensation. The data were zero-padded by a factor of two in all three dimensions to improve the visualization of the maximum-intensity projections (MIPs).

To quantify the level of contrast improvement achieved by the proposed technique, the mean signal levels were measured

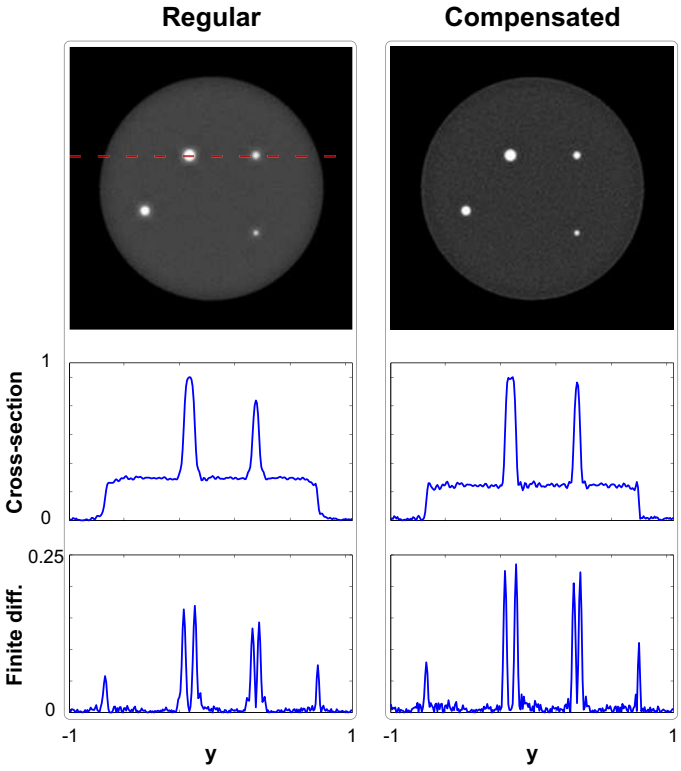

Fig. 5. Magnetization-prepared SSFP acquisitions of the numerical lower-leg phantom were simulated (N = 8). The data were reconstructed without and with compensation for the blood-signal decay, as shown in the left and right columns respectively. A sample cross-section across the dotted line is displayed for each image (middle row) along with its spatial-finite-differences transform (bottom row). The signal compensation considerably reduces the level of background muscle signal, and depicts the blood vessels with improved spatial resolution compared to the regular reconstruction. While the compensation significantly enhances the finite-differences peaks at the vessel edges, the background variation also increases due to amplified high-frequency noise. The success of the sparsity-based reconstruction inherently depends on the relative contributions of these two factors.

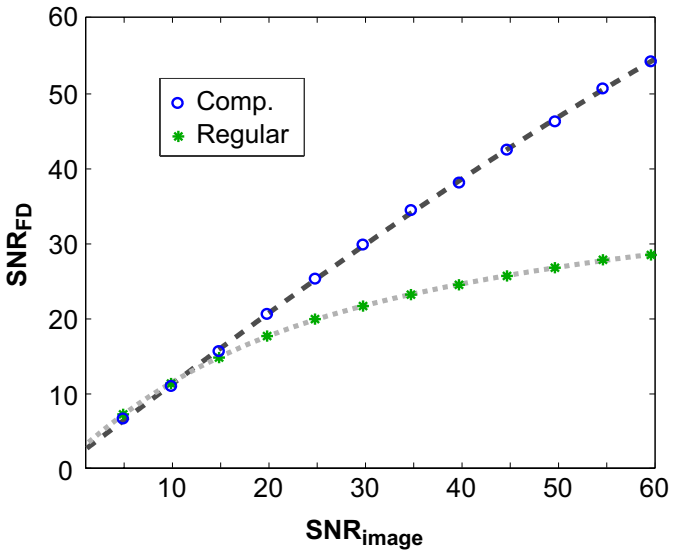

Fig. 6. Monte Carlo simulations were performed to analyze the effect of signal compensation on the performance of the sparsity-based reconstruction. The SNR in the spatial-finite-differences domain ($\mathrm{SNR_{FD}}$) is displayed as a function of the image SNR, for regular and compensated data. The circles and the stars represent the actual SNR levels, and the dashed lines are the corresponding fourth-order polynomial fits. While there are no significant differences at low $\mathrm{SNR_{image}}$, the compensated $\mathrm{SNR_{FD}}$ is higher ($\mathrm{p} < 10^{-6}$) for $\mathrm{SNR_{image}} > 12$. This indicates that signal compensation can potentially enhance the performance of the CS algorithm. In particular, the improvement in sparsity due to enhanced background suppression outweighs the adverse effects of noise amplification in this SNR range.

in identical regions of the source images reconstructed with CS. The blood signal was measured on the medial to distal segments of anterior/posterior tibial and peroneal arteries. The average diameters of the vessel lumens used in the measurements were approximately 2 mm. Meanwhile, neighboring regions of homogeneous signal were selected to measure the background muscle signal. Finally, the blood/muscle contrast was computed as the ratio of the mean blood signal to the mean muscle signal.

III. Results

The numerical lower-leg phantom images reconstructed without and with signal compensation are shown in Fig. 5. The compensated image looks sharper than the regular reconstruction. In addition, the background muscle signal is significantly reduced with the help of compensation. The blood/muscle contrast measurements in magnetization-prepared numerical phantom images are listed in Tables I, II, and III. Table I shows the variation of contrast with vessel diameter for N = 8. On the other hand, Table II demonstrates the effect of N for a fixed vessel diameter of 2 mm. As theoretically predicted, the compensation attains the highest levels of improvement for smaller vessel diameters and N. It is also important to note that the percentage contrast difference between the 1- and 4-mm vessels is reduced from 27.7% to 6.2% after compensation. Finally, the effects of $\mathrm{T_{1,2}}$ variations are listed in Table III for a 2-mm vessel, and N = 8. Whereas $\mathrm{T_2}$ perturbations (particularly for muscle) increase the standard deviation of contrast compared with variations in $\mathrm{T_1}$, both the contrast levels and percentage improvements with compensation are nearly identical to their nominal values. Therefore, the compensation filter is robust against such parameter variations.

Fig. 5 also displays the horizontal cross-sections and corresponding finite-differences (FD) transforms of the regular and compensated images. In the FD domain, the peaks near the blood vessels are higher and sharper due to the improvements in contrast and resolution with compensation. Furthermore, the plots of $\mathrm{SNR_{FD}}$ in Fig. 6 show that the increased peak levels outweigh the noise amplification ($\mathrm{p} < 10^{-6}$) for $\mathrm{SNR_{image}} > 12$. This suggests that the performance of CS reconstructions can be potentially enhanced with compensation as well. Meanwhile, the FD-domain SNRs for regular and compensated cases are nearly identical for lower $\mathrm{SNR_{image}}$.

Fig. 7 clearly demonstrates the effect of the proposed technique on spatial resolution. The regular PSF is widened due to the transient signal decay, and its peak amplitude is reduced. Meanwhile, the compensated PSF has a much narrower mainlobe as expected. Table IV lists the corresponding spatial resolutions. Whereas the image resolution in regular acquisitions is lowered to ~1.4 mm, the proposed technique

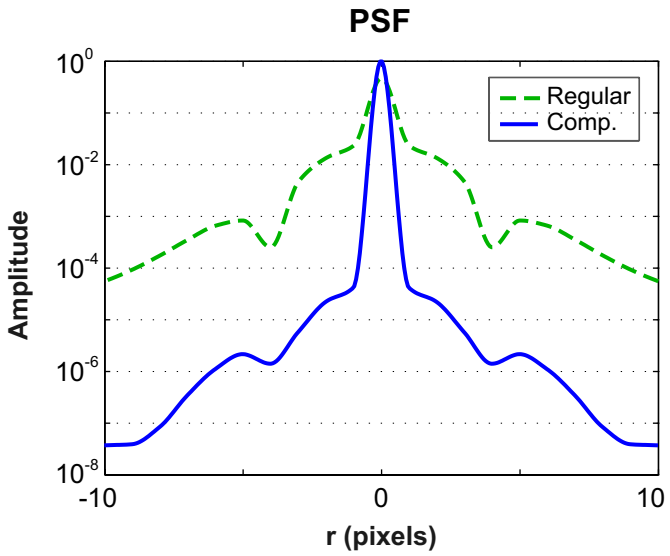

Fig. 7. Regular and compensated point spread functions (PSFs) were computed in the phase-encode dimensions by simulating the arterial-blood signal (T_1/T_2 = 1200/250 ms). Central cross sections of the PSFs are plotted in logarithmic scale. The regular PSF is widened and has a reduced peak amplitude due to the signal decay. On the other hand, the compensation significantly improves the signal homogeneity across k-space, and successfully maintains the nominal spatial resolution.

TABLE I
VARIATION OF BLOOD/MUSCLE CONTRAST WITH VESSEL DIAMETER

Vessel diameter	1 mm	2 mm	3 mm	4 mm
Regular	2.53	2.77	3.03	3.23
Compensated	3.70	3.77	3.88	3.93
% improvement	46.4%	36.1%	28.0%	21.7%

Blood/muscle contrast (i.e., the ratio of the mean signals) in regular and compensated numerical phantom images, measured in four vessels with intraluminal diameters varying from 1 to 4 mm. While the compensated contrast is always higher than the regular, the largest improvement is attained for smaller diameters due to the increased high-frequency content of small vessels.

TABLE II
BLOOD/MUSCLE CONTRAST IN REGULAR AND COMPENSATED PHANTOM IMAGES

Segments	N = 4	N = 8	N = 16
Regular	2.56	2.77	3.07
Compensated	3.70	3.77	3.85
% improvement	44.9%	36.1%	25.5%

Blood/muscle contrast in regular and compensated numerical phantom images, measured in a blood vessel (2 mm in diameter) for number of k-space segments (N) = 4, 8, and 16. As expected, the acquisition with the steepest magnetization decay over k-space (i.e., N = 4) benefits the most from signal compensation.

successfully maintains the nominal resolution of 1 mm in all cases.

As shown in Figs. 8 and 9, the proposed technique improves the contrast and resolution for both the fully-sampled and undersampled in vivo angiograms, enhancing the depiction of the vasculature. The Fourier and CS reconstructions alone of regular data yield suboptimal muscle suppression. Fig. 8 also displays the regular and signal-compensated angiograms without the CS reconstruction, which suffer from increased noise levels. Contrarily, the combination of CS with signal compensation generates high blood/background contrast and recovers the blood signal reliably by reducing the image noise.

Table V lists the measurements of in vivo blood/muscle contrast. The proposed technique achieves significantly improved contrast (up to 48%) in all datasets, but the highest levels of improvement are observed for smaller N and R. The contrast measurements in fully-sampled angiograms (Table V) have similar values to those in the numerical phantom (Table II). Furthermore, the corresponding percentage improvements due to compensation are nearly identical. It is important to note that the proposed technique achieves enhanced resolution and contrast with shorter scan times and lower accelerations compared to regular acquisitions. For example, the compensated contrast for N = 4 is higher than the regular contrast for N = 16, although N = 16 requires a 56%-longer total scan time.

IV. DISCUSSION

The proposed technique enhances the resolution and contrast of magnetization-prepared acquisitions by signal compensation. Afterward, the image noise and aliasing artifacts are reduced with the help of CS, allowing more reliable depiction of the underlying tissue signal. The technique substantially improves the visualization of the vasculature in non-contrast-enhanced peripheral SSFP angiograms.

Limitations

Whereas the increase in resolution with the proposed technique can be readily anticipated, the contrast improvement arises due to the lower spatial-frequency content of the background. Because this improvement depends on the relative spectral widths of the sample tissues, the signal of smaller vessels will benefit more than that of larger vasculature. However, we have not observed any loss in image quality for large vessels due to this effect. In fact, the compensation produces more homogeneous contrast for varying vessel sizes (Table I), yielding more consistent and reliable visualization.

The phantom and in vivo measurements indicated nearly identical percentage improvements in contrast, but the contrast values themselves were slightly different. Several factors might have led to these minor discrepancies. First, the muscle signal in short-TR SSFP acquisitions is further reduced due to magnetization-transfer effects [41], increasing the in vivo blood/muscle contrast. Furthermore, in vivo $T_{1,2}$ values can be potentially different from the simulated values.

The amplification of high spatial frequencies can lead to edge enhancement in certain tissues, which experience a smaller signal change between the preparation and steady state compared to the tissue of interest. While some level of edge enhancement was visible in the simulations for muscle tissue, its signal is much smaller compared to that of blood. Furthermore, no significant artifacts were observed in vivo

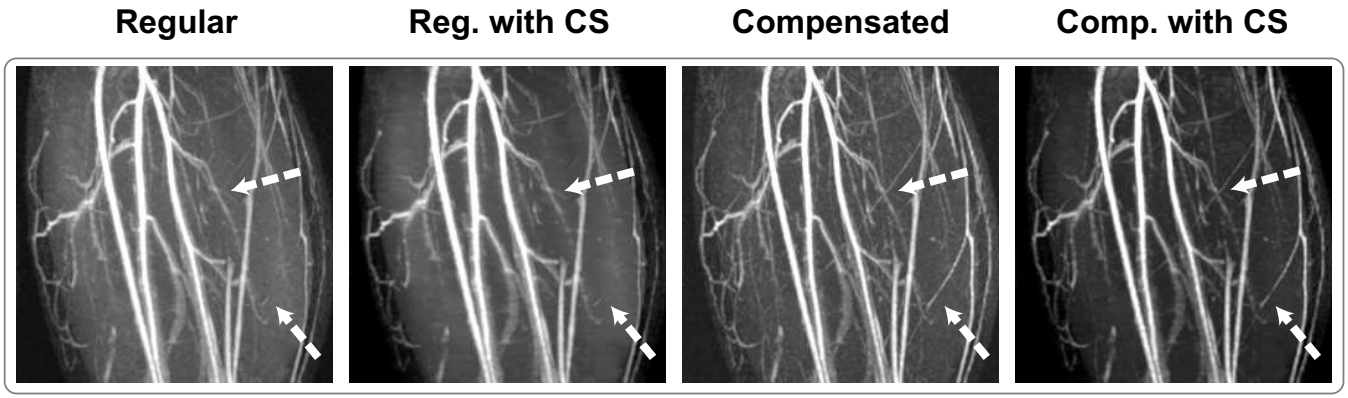

Fig. 8. Regular and signal-compensated images of fully-sampled data (R = 1, N = 8): **(a)** maximum-intensity projections (MIPs), and **(b)** axial slices. Both regular and compensated datasets were processed with Fourier and compressed-sensing (CS) reconstructions separately. Images of regular data suffer from blurring due to the transient signal decay. Meanwhile, the Fourier reconstruction of compensated data has improved resolution at the expense of amplified noise. Finally, CS successfully reduces the noise in the compensated images, which look sharper and have improved background suppression compared to the regular case. The arrows pinpoint a number of small vessel branches that are not visible in the regular MIPs. Contrarily, these vessels are clearly visualized with the enhanced contrast and spatial resolution of the compensated reconstructions.

TABLE III
SIMULATED BLOOD/MUSCLE CONTRAST WITH VARIATIONS IN RELAXATION PARAMETERS

Variation	$T_{1m}^{spatial}$	T_{1m}	T_{1b}	T_{2b}	T_{2m}	$T_{2m}^{spatial}$	Combined
Regular	2.74±0.11	2.74±0.18	2.76±0.18	2.74±0.25	2.83±0.46	2.84±0.64	2.84±0.66
Compensated	3.75±0.16	3.74±0.25	3.77±0.26	3.74±0.37	3.88±0.71	3.87±0.81	3.87±0.89
% improvement	36.8±2.6%	36.6±2.7%	36.8±3.0%	36.5±3.4%	36.9±4.1%	36.5±2.3%	36.4±3.9%

Relaxation parameters for blood and muscle ($T_{1,2m}$ and $T_{1,2b}$) were individually varied by ±20% in numerical phantom images. The superscript 'spatial' indicates that the parameter was varied spatially instead of changing the value of the entire block of tissue. Blood/muscle contrast was measured in a blood vessel (2 mm in diameter) for 8 k-space segments. The mean and standard deviation across the range of varied parameters are listed for each measurement. The combined simulation was performed by independently varying four parameters: T_{1m}, T_{1b}, T_{2b}, and $T_{2m}^{spatial}$.

despite the shorter T_2 of muscle, possibly due to its lower frequency content. When background tissues with considerable high-frequency content are insufficiently suppressed, partial decay compensation can help prevent edge enhancement [42].

Comparison to Existing Methods

Several other strategies are often used to improve the performance of magnetization-prepared imaging. First of all, the background can be better suppressed by shortening the readout clusters (i.e., increasing N). However, the data acquisition becomes less efficient, and prolonged scan times can yield increased sensitivity to motion artifacts. When high-energy RF pulses are employed (e.g., adiabatic pulses), frequent preparation also results in increased specific absorption rates and limits the applicability at high field strengths.

Meanwhile, various techniques have been previously proposed to enhance the spatial resolution in transient acquisitions. On the one hand, variable-flip-angle trains can yield more consistent signal across k-space to prevent image blurring [8], [17], [43]. Although signal homogeneity is maintained, this scheme reduces the overall signal levels. Furthermore, different trains need to be designed for various imaging conditions, increasing the susceptibility to B_1 inhomogeneities.

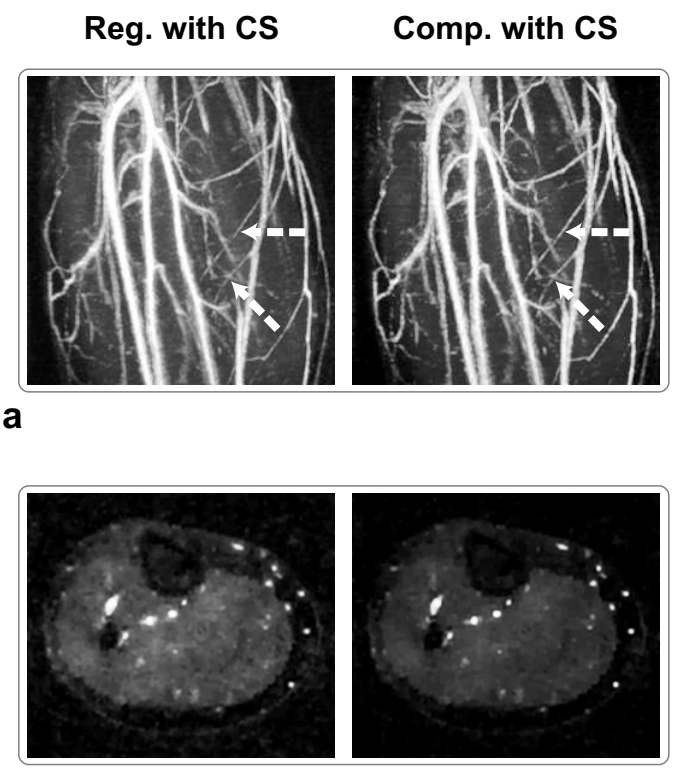

Fig. 9. **(a)** MIPs and **(b)** axial images of regular and signal-compensated CS reconstructions, from undersampled (R = 2, N = 8) data. As predicted by the results in Fig. 6, CS demonstrates enhanced performance in noise/artifact removal on compensated images, which have enhanced resolution and decreased background signal. The arrows point to the small vessels that are more visibly depicted in the compensated MIPs due to the superior background suppression.

On the other hand, specialized postprocessing methods have been successfully employed to compensate for the transient signal decay [44]–[46]. These methods often estimate the relaxation constants at each pixel for a more accurate correction. However, because the reconstructions do not include a denoising step, their use is mostly limited to high-SNR imaging scenarios. As a remedy, the high-frequency noise has been dampened by weighting the k-space correction filter with a low-pass window [47], [48]. While the level of noise amplification is reduced, the ideal PSF and spatial resolution cannot be preserved with this strategy.

The proposed technique fully compensates the signal decay to maintain the prescribed nominal resolution, and reduces the resulting noise with CS reconstructions. Similar to other postprocessing approaches, it does not require any modification of the scan parameters or the imaging sequence. The tissue/background contrast is improved without sacrificing scan efficiency. Furthermore, the technique offers enhanced applicability at higher field strengths along with improved robustness against RF field inhomogeneities compared to existing techniques. It may potentially benefit other applications, where the initially prepared contrast is gradually replaced with a lower steady-state contrast (e.g., T_2-prepared [49], $T_{1\rho}$ [50], and hyperpolarized imaging [51]).

TABLE IV
SPATIAL RESOLUTION FOR REGULAR AND COMPENSATED IMAGES

Segments	N = 4	N = 8	N = 16
Regular	1.46	1.43	1.39
Compensated	0.99	0.99	0.99

Estimated isotropic spatial resolution (in mm) in the phase-encode plane for regular acquisitions and compensated images. In the regular images, the largest loss in resolution occurs with the smallest number of k-space segments (N). In all cases, compensating for the signal decay prevents image blurring by maintaining the nominal image resolution of 1 mm.

Potential Improvements

There are potential variations that can help improve the proposed technique. First, when the signal decays very rapidly, full compensation may deteriorate the image quality due to high noise amplification. In such cases, variable-flip-angle trains can be used to partially improve the signal homogeneity, while the remaining decay can still be corrected with postprocessing [52]. This hybrid can further extend the applicability of the technique by reducing the overall image noise. Furthermore, the k-space correction filter is computed from the relaxation parameters of a single tissue of interest. When the signal from heterogeneous samples need to be compensated, improved methods that estimate the spatially varying relaxation parameters can be incorporated [44]–[46].

The nonlinear reconstructions in the CS framework rely on iterative computations that are relatively intensive. Reducing the complexity of such reconstructions is an active field of research, and the proposed technique can potentially benefit from further developments in this field [20]. In applications where the data are not compressible in the image domain, the TV regularization term in CS reconstructions can be replaced with an appropriate sparsifying transform (e.g., wavelet transform). CS can also be replaced with a combination of parallel imaging [11], [12] and specialized denoising methods [36], and the use of this combination in conjunction with the proposed technique should be straightforward. Partial Fourier imaging is yet another acceleration technique, e.g., partial echo acquisitions can be employed to improve the spatial resolution in the readout direction without affecting the TR of the host sequence. Nevertheless, the scan-time savings and the reconstruction quality might be limited by undesirable phase shifts due to field inhomogeneities, eddy currents, and patient motion [35].

V. CONCLUSION

Magnetization-prepared acquisitions often require prolonged scan times and suffer from image blurring. The proposed technique enhances the image contrast and resolution through simple postprocessing of the collected data, while maintaining high scan efficiency. Therefore, it improves the robustness and applicability of magnetization-prepared imaging, particularly when scan times are constrained. These improvements were quantitatively demonstrated in theoretical

TABLE V
BLOOD/MUSCLE CONTRAST IN REGULAR AND COMPENSATED IN VIVO IMAGES

Fully-sampled	**N = 4**	**N = 8**	**N = 16**
Regular	2.68	3.30	3.55
Compensated	3.96	4.08	4.50
% improvement	47.8%	37.0%	26.9%

Undersampled	**R = 1**	**R = 2**	**R = 4**
Regular	2.68	3.39	3.96
Compensated	3.96	4.60	4.70
% improvement	47.8%	35.9%	18.9%

Blood/muscle contrast in regular and compensated in vivo images (both reconstructed with CS) for fully-sampled and undersampled acquisitions. The largest improvement with compensation is for smaller N and undersampling factors (R). The compensated contrast for N = 4 is higher than the regular contrast for N = 16, although N = 16 requires a 56%-longer total scan time.

simulations and in vivo non-contrast-enhanced peripheral angiograms.

REFERENCES

[1] J. Frahm, A. Haase, and D. Matthaei, "Rapid NMR imaging of dynamic processes using the FLASH technique." *Magn Reson Med*, vol. 3, no. 2, pp. 321–327, 1986.

[2] J. H. den Boef, C. M. van Uijen, and C. D. Holzscherer, "Multiple-slice NMR imaging by three-dimensional Fourier zeugmatography." *Phys Med Biol*, vol. 29, no. 7, pp. 857–867, 1984.

[3] R. R. Edelman, W. J. Manning, D. Burstein, and S. Paulin, "Coronary arteries: breath-hold MR angiography." *Radiology*, vol. 181, no. 3, pp. 641–643, 1991.

[4] C. H. Meyer, B. S. Hu, D. G. Nishimura, and A. Macovski, "Fast spiral coronary artery imaging," *Magn Reson Med*, vol. 28, no. 2, pp. 202–213, 1992.

[5] M. R. Prince, "Gadolinium-enhanced MR aortography." *Radiology*, vol. 191, no. 1, pp. 155–164, 1994.

[6] S. Ogawa, T. M. Lee, A. S. Nayak, and P. Glynn, "Oxygenation-sensitive contrast in magnetic resonance image of rodent brain at high magnetic fields." *Magn Reson Med*, vol. 14, no. 1, pp. 68–78, 1990.

[7] M. S. Albert, G. D. Cates, B. Driehuys, W. Happer, B. Saam, C. S. Springer, and A. Wishnia, "Biological magnetic resonance imaging using laser-polarized ^{129}Xe." *Nature*, vol. 370, no. 6486, pp. 199–201, 1994.

[8] L. Zhao, R. Mulkern, C. H. Tseng, D. Williamson, S. Patz, R. Kraft, R. L. Walsworth, F. A. Jolesz, and M. S. Albert, "Gradient-echo imaging considerations for hyperpolarized ^{129}Xe MR." *J Magn Reson B*, vol. 113, pp. 179–183, 1996.

[9] E. E. de Lange, S. R. Urbanski, J. P. Mugler, and J. R. Brookeman, "Magnetization-prepared rapid gradient echo (MP-RAGE) magnetic resonance imaging of Morgagni's hernia." *Eur J Radiol*, vol. 11, no. 3, pp. 196–199, 1990.

[10] J. P. Mugler and J. R. Brookeman, "Three-dimensional magnetization-prepared rapid gradient-echo imaging (3D MP RAGE)." *Magn Reson Med*, vol. 15, no. 1, pp. 152–157, 1990.

[11] R. M. Heidemann, O. Ozsarlak, P. M. Parizel, J. Michiels, B. Kiefer, V. Jellus, M. Muller, F. Breuer, M. Blaimer, M. A. Griswold, and P. M. Jakob, "A brief review of parallel magnetic resonance imaging," *Eur Radiol*, vol. 13, no. 6, pp. 2323–2337, 2003.

[12] K. P. Pruessmann, "Encoding and reconstruction in parallel MRI." *NMR Biomed*, vol. 19, no. 3, pp. 288–299, 2006.

[13] A. E. Holsinger and S. J. Riederer, "The importance of phase-encoding order in ultra-short TR snapshot MR imaging." *Magn Reson Med*, vol. 16, no. 3, pp. 481–488, 1990.

[14] A. E. Bampton, S. J. Riederer, and H. W. Korin, "Centric phase-encoding order in three-dimensional MP-RAGE sequences: application to abdominal imaging." *J Magn Reson Imaging*, vol. 2, no. 3, pp. 327–334, 1992.

[15] A. H. Wilman and S. J. Riederer, "Performance of an elliptical centric view order for signal enhancement and motion artifact suppression in breath-hold three-dimensional gradient echo imaging," *Magn Reson Med*, vol. 38, pp. 793–802, 1997.

[16] J. M. Wild, M. N. J. Paley, M. Viallon, W. G. Schreiber, E. J. R. van Beek, and P. D. Griffiths, "k-space filtering in 2D gradient-echo breath-hold hyperpolarized ^{3}He MRI: spatial resolution and signal-to-noise ratio considerations." *Magn Reson Med*, vol. 47, no. 4, pp. 687–695, 2002.

[17] J. P. Mugler, F. H. Epstein, and J. R. Brookeman, "Shaping the signal response during the approach to steady state in three-dimensional magnetization-prepared rapid gradient-echo imaging using variable flip angles." *Magn Reson Med*, vol. 28, no. 2, pp. 165–185, 1992.

[18] L. I. Rudin, S. Osher, and E. Fatemi, "Nonlinear total variation based noise removal algorithms," *Physica D*, vol. 60, pp. 259–268, 1992.

[19] K. T. Block, M. Uecker, and J. Frahm, "Undersampled radial MRI with multiple coils: Iterative image reconstruction using a total variation constraint," *Magn Reson Med*, vol. 57, pp. 1086–1098, 2007.

[20] M. Lustig, D. Donoho, and J. M. Pauly, "Sparse MRI: The application of compressed sensing for rapid MR imaging," *Magn Reson Med*, vol. 58, no. 6, pp. 1182–1195, 2007.

[21] G. A. Wright, D. G. Nishimura, and A. Macovski, "Flow-independent magnetic resonance projection angiography," *Magn Reson Med*, vol. 17, no. 1, pp. 126–140, 1991.

[22] J. H. Brittain, E. W. Olcott, A. Szuba, G. E. Gold, G. A. Wright, P. Irarrazaval, and D. G. Nishimura, "Three-dimensional flow-independent peripheral angiography," *Magn Reson Med*, vol. 38, no. 3, pp. 343–354, 1997.

[23] E. Kanal, A. J. Barkovich, C. Bell, J. P. Borgstede, W. G. Bradley, J. W. Froelich, T. Gilk, J. R. Gimbel, J. Gosbee, E. Kuhni-Kaminski, J. W. Lester, J. Nyenhuis, Y. Parag, D. J. Schaefer, E. A. Sebek-Scoumis, J. Weinreb, L. A. Zaremba, P. Wilcox, L. Lucey, and N. Sass, "ACR guidance document for safe MR practices: 2007," *AJR Am J Roentgenol*, vol. 188, no. 6, pp. 1447–1474, 2007.

[24] T. Çukur, M. Lustig, and D. G. Nishimura, "Improving non-contrast-enhanced steady-state free precession angiography with compressed sensing," *Magn Reson Med*, vol. 61, no. 5, pp. 1122–1131, 2009.

[25] N. K. Bangerter, B. A. Hargreaves, J. H. Brittain, B. Hu, S. S. Vasanawala, and D. G. Nishimura, "3D fluid-suppressed T_2-prep flow-independent angiography using balanced SSFP," in *Proceedings of the 12th Annual Meeting of ISMRM*, Kyoto, 2004, p. 11.

[26] T. Çukur, J. H. Lee, N. K. Bangerter, B. A. Hargreaves, and D. G. Nishimura, "Non-contrast-enhanced flow-independent peripheral MR angiography with balanced SSFP," *Magn Reson Med*, vol. 61, no. 6, pp. 1533–1539, 2009.

[27] J. Leupold, J. Hennig, and K. Scheffler, "Alternating repetition time balanced steady state free precession," *Magn Reson Med*, vol. 55, pp. 557–565, 2006.

[28] R. Nezafat, R. Ouwerkerk, A. J. Derbyshire, M. Stuber, and E. R. McVeigh, "Spectrally selective B_1-insensitive T_2 magnetization preparation sequence." *Magn Reson Med*, vol. 61, no. 6, pp. 1326–1335, 2009.

[29] H. W. Korin, S. J. Riederer, A. E. H. Bampton, and R. L. Ehman, "Altered phase encoding order for reduced sensitivity to motion corruption in 3DFT MR imaging," *J Magn Reson Imaging*, vol. 2, no. 1, pp. 687–693, 1992.

[30] B. A. Hargreaves, S. S. Vasanawala, J. M. Pauly, and D. G. Nishimura, "Characterization and reduction of the transient response in steady-state MR imaging," *Magn Reson Med*, vol. 46, no. 1, pp. 149–158, 2001.

[31] P. Le Roux, "Simplified model and stabilization of SSFP sequences," *J Magn Reson*, vol. 163, no. 1, pp. 23–37, 2003.

[32] K. Scheffler, "On the transient phase of balanced SSFP sequences." *Magn Reson Med*, vol. 49, no. 4, pp. 781–783, Apr 2003. [Online]. Available: http://dx.doi.org/10.1002/mrm.10421

[33] R. L. Greenman, J. E. Shirosky, R. V. Mulkern, and N. M. Rofsky, "Double inversion black-blood fast spin-echo imaging of the human heart: A comparison between 1.5T and 3.0T," *J Magn Reson Imaging*, vol. 17, pp. 648–655, 2003.

[34] R. M. Botnar, M. Stuber, P. G. Danias, K. V. Kissinger, and W. J. Manning, "Improved coronary artery definition with T_2-weighted, free-breathing, three-dimensional coronary MRA." *Circulation*, vol. 99, no. 24, pp. 3139–3148, 1999.

[35] M. A. Bernstein, K. F. King, and X. J. Zhou, *Handbook of MRI pulse sequences*, 1st ed. Burlington, MA: Elsevier Academic Press, 2004.

[36] A. Buades, B. Coll, and J. M. Morel, "A review of image denoising algorithms, with a new one," *Multisc Model Simulat*, vol. 4, no. 2, pp. 490–530, 2005.
[37] B. I. Mazhbich, "Noninvasive determination of elastic properties and diameter of human limb arteries." *Pflugers Arch*, vol. 396, no. 3, pp. 254–259, 1983.
[38] A. J. Narracott, G. W. John, D. R. Hose, R. J. Morris, J. P. Woodcock, and P. V. Lawford, "Influence of intermittent compression cuff design on calf deformation: computational results." *Conf Proc IEEE Eng Med Biol Soc*, vol. 2007, pp. 6334–6338, 2007.
[39] J. G. Pipe, "Reconstructing MR images from undersampled data: Data-weighting considerations," *Magn Reson Med*, vol. 43, pp. 867–875, 2000.
[40] J. D. Robson, *Applied Multivariate Data Analysis*, 4th ed. New York, NY: Springer-Verlag, 1991, vol. 1.
[41] O. Bieri and K. Scheffler, "On the origin of apparent low tissue signals in balanced SSFP," *Magn Reson Med*, vol. 56, pp. 1067–1074, 2006.
[42] R. F. Busse, S. J. Riederer, J. G. Fletcher, A. E. Bharucha, and K. R. Brandt, "Interactive fast spin-echo imaging." *Magn Reson Med*, vol. 44, no. 3, pp. 339–348, Sep 2000.
[43] X. Li, E. T. Han, R. F. Busse, and S. Majumdar, "In vivo $T_{1\rho}$ mapping in cartilage using 3D magnetization-prepared angle-modulated partitioned k-space spoiled gradient echo snapshots (3D MAPSS)." *Magn Reson Med*, vol. 59, no. 2, pp. 298–307, 2008.
[44] I. Shenberg and A. Macovski, "Resolution and noise considerations in MRI systems with time-varying gradients." *IEEE Trans Med Imaging*, vol. 4, no. 3, pp. 144–152, 1985.
[45] K. Oshio and M. Singh, "A computer simulation of T_2 decay effects in echo planar imaging." *Magn Reson Med*, vol. 11, no. 3, pp. 389–397, 1989.
[46] X. Zhou, Z. P. Liang, G. P. Cofer, C. F. Beaulieu, S. A. Suddarth, and G. A. Johnson, "Reduction of ringing and blurring artifacts in fast spin-echo imaging." *J Magn Reson Imaging*, vol. 3, no. 5, pp. 803–807, 1993.
[47] R. F. Busse, S. J. Riederer, J. G. Fletcher, A. E. Bharucha, and K. R. Brandt, "Interactive fast spin-echo imaging," *Magn Reson Med*, vol. 44, no. 3, pp. 339–348, 2000.
[48] W. R. T. Witschey, A. Borthakur, M. A. Elliott, M. Fenty, M. A. Sochor, C. Wang, and R. Reddy, "$T_{1\rho}$-prepared balanced gradient echo for rapid 3D $T_{1\rho}$ MRI." *J Magn Reson Imaging*, vol. 28, no. 3, pp. 744–754, 2008.
[49] J. H. Brittain, B. S. Hu, G. A. Wright, C. H. Meyer, A. Macovski, and D. G. Nishimura, "Coronary angiography with magnetization-prepared T_2 contrast," *Magn Reson Med*, vol. 33, no. 5, pp. 689–696, 1995.
[50] A. C. Nugent and G. A. Johnson, "$T_{1\rho}$ imaging using magnetization-prepared projection encoding (MaPPE)." *Magn Reson Med*, vol. 43, no. 3, pp. 421–428, 2000.
[51] H. Middleton, R. D. Black, B. Saam, G. D. Cates, G. P. Cofer, R. Guenther, W. Happer, L. W. Hedlund, G. A. Johnson, and K. Juvan, "MR imaging with hyperpolarized ^{3}He gas." *Magn Reson Med*, vol. 33, no. 2, pp. 271–275, 1995.
[52] R. F. Busse, "Designing variable flip angle refocusing trains to optimize resolution, signal-to-noise, and rf power." in *Proceedings of the 13th Annual Meeting of ISMRM*, Miami Beach, 2005, p. 2349.